

Transport modeling of sedimenting particles in a turbulent pipe flow using Euler-Lagrange large eddy simulation

Sunil K. Arolla^{a,*}, Olivier Desjardins^a

^a*Sibley School of Mechanical and Aerospace Engineering, Cornell University, Ithaca, NY 14853, USA*

Abstract

A volume-filtered Euler-Lagrange large eddy simulation methodology is used to predict the physics of turbulent liquid-solid slurry flow through a horizontal pipe. A dynamic Smagorinsky model based on Lagrangian averaging is employed to account for the sub-filter scale effects in the liquid phase. A fully conservative immersed boundary method is used to account for the pipe geometry on a uniform cartesian grid. The liquid and solid phases are coupled through volume fraction and momentum exchange terms. Particle-particle and particle-wall collisions are modeled using a soft-sphere approach. A series of simulations have been performed by varying the superficial liquid velocity to be consistent with the experimental data by Dahl et al. (2003). Depending on the liquid flow rate, a particle bed can form and develop different patterns, which are discussed in the light of various regime diagrams proposed in the literature. The fluctuation in the height of the liquid-bed interface is characterized to understand the space and time evolution of these patterns. Mean flow statistics of engineering interest such as mean velocity, mean concentration, and mean streamwise pressure gradient driving the flow are extracted from the numerical simulations and presented. Sand hold-up calculated from the simulation results suggest that this computational strategy is capable of predicting critical deposition velocity accurately.

Keywords: liquid-solid slurry, sediment transport, dune formation,

*Corresponding author

Email addresses: `ska62@cornell.edu` (Sunil K. Arolla),
`olivier.desjardins@cornell.edu` (Olivier Desjardins)

1. Introduction

Turbulent liquid-solid flows have a wide range of applications such as in the long distance transport of bulk materials to the processing plants and in the geomorphology where sediment may be entrained, transported, and deposited by water flow. Of particular interest in this work is the transport of oil sand through pipelines. In a near-horizontal pipeline, depending on the liquid flow rate, the slurry flow can exhibit four main regimes. At low liquid flow rates, the sand sediments to the bottom of the pipe and forms a stable, stationary bed. When the liquid flow rate increases above a specific value, the sand starts getting transported in a thin layer above the bed. As the flow rate increases further, the sand bed breaks into a series of slow-moving dunes, which eventually grow to develop into bed moving along the bottom of the pipe. At even higher flow rates, the sand particles ultimately become fully suspended in the carrier liquid. The velocity at the onset of a stationary bed formation is referred to as the critical deposition velocity. The formation of a stationary sand bed can pose several risks such as increased frictional losses, possibility of microbially-induced corrosion under the sand bed, and equipment failure due to sand accumulation. So, predicting the critical deposition velocity and understanding the physics of liquid-solid pipe flows is important for the efficient design of of slurry pipelines. Moreover, the interaction between the turbulent carrier flow and a dense sediment layer has relevance in the sediment transport modeling as well.

The response of a bed of particles to shearing flows has been widely studied in the context of the formation of alluvial river channels (Church, 2006). There are four dimensionless parameters that are used to parameterize the transport of sedimenting particles, the choice of which is non-unique (Yalin, 1977). The first parameter that represents the incipient motion of particles is called the Shields number, $\theta = \tau_b / (\rho_p - \rho_f) g d_p$, where τ_b is the shear stress at the bed surface, d_p is the particle diameter, and ρ_p and ρ_f are the density of the solid and fluid, respectively. This parameter measures the relative importance of the destabilizing hydrodynamic force over the stabilizing gravity force. The threshold value for particle motion is denoted as the critical Shields number (θ_c). The second parameter is the specific gravity of the solid particles, $s = \rho_p / \rho_f$. The third dimensionless parameter usually involves the

fluid height, h_f/d_p , or a Froude number, $Fr = \sqrt{\tau_b/(\rho_f g h_f)}$. The fourth parameter used is called the fall parameter, $R_p = d_p \sqrt{(s-1)g}/\nu$, which represents the relative importance of the gravity and the viscosity of the fluid (Jenkins and Hanes, 1998). The experimental data collected in the turbulent flow with sedimenting particles are conventionally represented in a *Shields diagram* with the Shields number as ordinate and fall parameter as abscissa. This curve is used to distinguish different modes of sediment transport as well as type of bedforms. When the flow is too weak to induce sediment motion ($\theta < \theta_c$), bedforms will be usually determined by previous stronger events (Nielsen, 1992). For flows such that $\theta_c < \theta < 0.8$, bedforms such as vortex ripples or dunes will be present. For more intense flows with $\theta > 0.8$, bedforms disappear and flat beds are observed in a regime called sheet flow. This criterion for sheet flow inception is proposed by Wilson (1989) while there are other criteria and formulas exist in the literature. Most of the data available in the turbulent regime for threshold of particle motion present large scatters due to systematic methodological biases of incipient motion of the bed (Buffington and Montgomery, 1997; Vanoni, 1946; Dancey et al., 2002; Paintal, 1971). The threshold values determined from the bedload transport rate are usually larger than those deduced from the visual observations of the particle motion. This discrepancy is largely due to differences between the initial state of the bed as erosion and deposition are very sensitive to the bed packing conditions (Papnicolaou et al., 2002). This is particularly important to acknowledge when validating computational methods against the data. The presumably simpler laminar flow also suffers from the same difficulty. Recent work of Ouriemi et al. (2007), and Peysson et al. (2009) attempted to address this by providing robust and reproducible experimental measurements to infer critical Shields number.

The type of bedform significantly influences the flow characteristics such as resistance, mixing properties and importantly, characteristics such as thickness of the transport layer. So, it is highly desirable to be able to predict the nature of bedforms from an engineering point of view. It is now generally accepted that the mechanism that destabilizes a flat sediment bed is the phase lag between the perturbation in bed height and the bottom shear stress (Charru, 2006). Linear stability analysis is often applied to the problem in order to predict the most unstable wavelength, but this approach is not found to be satisfactory with pattern wavelength prediction sometimes off by an order of magnitude (Raudkivi, 1997; Langlois and Valance, 2007;

Coleman and Nikora, 2009; Ouriemi et al., 2009a). Experimentally, a closed pipe configuration is ideal for such investigations as it offers a confined, well-controlled flow. A phase diagram showing different dune patterns observed when a bed composed of spherical particles in a pipe flow is presented by Ouriemi et al. (2009b). They showed that dune formation is controlled by Reynolds number while the incipient motion of particles is controlled by the Shields number.

With increasing computational resources and advancements in numerical methods, computational fluid dynamics (CFD) provides a unique opportunity to understand the physics of liquid-solid pipe flows for a range of liquid flow rates. The Navier-Stokes are the governing equations for the carrier liquid phase, but it is not practical to resolve wide range of scales in a turbulent flow. Moreover, resolving the flow around each particle becomes overly expensive. In a recent work, Capecelatro and Desjardins (2013a) developed an Euler-Lagrange large eddy simulation (LES) framework in which the background carrier flow is solved using a volume-filtered LES methodology while each particle is tracked for its position and velocity in a Lagrangian approach. This methodology showed unique capability to predict particle bed formation and excellent agreement with the experimental data was obtained for a case with the liquid velocity above the critical deposition velocity (Capecelatro and Desjardins, 2013b). This framework can be used to explore the physics of liquid-solid slurry flows at Reynolds numbers of practical interest. To the best of our knowledge, no attempt to numerically simulate the evolution of bed of particles in a turbulent flow leading to the pattern formation at high Reynolds numbers has been reported to date. Notably, Kidanemariam and Uhlmann (2014) presented results from fully resolved direct numerical simulations (DNS) in a channel flow configuration, but the highest Reynolds number based on bulk velocity is 6022. While their work demonstrated the feasibility of using fully resolved DNS for studying sediment pattern formation, the computational cost required was enormous and moreover, computational domain size chosen is too restrictive to resolve the large scale features occurring at high Reynolds numbers.

In this work, a volume-filtered Euler-Lagrange LES framework is applied to perform slurry flow simulations with different superficial liquid velocities and with the initial particle configuration set-up based on the sand hold-up data presented in (Danielson, 2007; Yang et al., 2006; Dahl et al., 2003). In contrast to the recent work by Kidanemariam and Uhlmann (2014), the flow is resolved on a grid that is of the same order of magnitude as that of the

particle diameter and the momentum exchange is modeled via a drag term. However, a full description of contact mechanics is retained through the use of soft-sphere collision model. The specific objectives in this work are 1) to establish the feasibility of Euler-Lagrange LES in the context of turbulent transport of sedimenting particles, 2) to compare predicted bedforms with that suggested by the data from the literature, and 3) to validate global flow quantities such as mean streamwise pressure gradient and critical deposition velocity with the experimental data of Dahl et al. (2003).

In the previous work by Capecelatro and Desjardins (2013b), validation of Euler-Lagrange LES strategy above the critical deposition velocity is presented and the feasibility of using this method for predicting static bed formation is demonstrated. Here, the focus is on validating this method below the critical deposition velocity and exploring the bedforms appearing in this regime.

2. Volume-filtered Euler-Lagrange LES framework

To solve the equations of motion for the liquid phase without requiring to resolve the flow around individual particles, a volume filtering operator is applied to the Navier-Stokes equations, thereby replacing the point variables (fluid velocity, pressure, etc.) by smoother, locally filtered fields. The volume-filtered continuity equation is given by

$$\frac{\partial}{\partial t} (\varepsilon_f \rho_f) + \nabla \cdot (\varepsilon_f \rho_f \mathbf{u}_f) = 0, \quad (1)$$

where ε_f , ρ_f , and \mathbf{u}_f are the fluid-phase volume fraction, density, and velocity, respectively. The momentum equation is given by

$$\frac{\partial}{\partial t} (\varepsilon_f \rho_f \mathbf{u}_f) + \nabla \cdot (\varepsilon_f \rho_f \mathbf{u}_f \otimes \mathbf{u}_f) = \nabla \cdot (\boldsymbol{\tau} - \mathbf{R}_u) + \varepsilon_f \rho_f \mathbf{g} - \mathbf{F}^{\text{inter}} + \mathbf{F}^{\text{mfr}}, \quad (2)$$

where \mathbf{g} is the acceleration due to gravity, $\mathbf{F}^{\text{inter}}$ is the interphase exchange term that arises from filtering the divergence of the stress tensor, and \mathbf{F}^{mfr} is a body force akin to a mean pressure gradient introduced to maintain a constant flow rate in the pipe. The volume-filtered stress tensor, $\boldsymbol{\tau}$, is expressed as

$$\boldsymbol{\tau} = -p\mathcal{I} + \mu \left[\nabla \mathbf{u}_f + \nabla \mathbf{u}_f^\top - \frac{2}{3} (\nabla \cdot \mathbf{u}_f) \mathcal{I} \right] + \mathbf{R}_\mu, \quad (3)$$

where the hydrodynamic pressure and dynamic viscosity are given by p and μ , respectively. \mathcal{I} is the identity tensor. \mathbf{R}_μ is an unclosed term that arises as a result of filtering the velocity gradients in the point wise stress tensor, and is modeled by introducing an effective viscosity μ^* to account for enhanced dissipation by the particles, given by

$$\mathbf{R}_\mu \approx \mu^* \left[\nabla \mathbf{u}_f + \nabla \mathbf{u}_f^\top - \frac{2}{3} (\nabla \cdot \mathbf{u}_f) \mathcal{I} \right], \quad (4)$$

where μ^* is taken from Gibilaro et al. (2007) for fluidized beds, and is given by

$$\mu^* = \mu (\varepsilon_f^{-2.8} - 1). \quad (5)$$

\mathbf{R}_u is a sub-filter Reynolds stress term closed through a turbulent viscosity model, given by

$$\mathbf{R}_u \approx \mu_t [\nabla \mathbf{u}_f + \nabla \mathbf{u}_f^\top]. \quad (6)$$

A dynamic Smagorinsky model (Germano et al., 1991; Lilly, 1992) based on Lagrangian averaging (Meneveau et al., 1996) is employed to estimate the turbulent viscosity μ_t .

A Lagrangian particle-tracking approach is used for the solid phase. The displacement of an individual solid particle indicated by the subscript p is calculated using Newton's second law of motion,

$$m_p \frac{d\mathbf{u}_p}{dt} = \mathbf{f}_p^{\text{inter}} + \mathbf{F}_p^{\text{col}} + m_p \mathbf{g}, \quad (7)$$

where the particle mass is defined by $m_p = \pi \rho_p d_p^3 / 6$, where ρ_p and d_p are the particle density and diameter, respectively. The force $\mathbf{f}_p^{\text{inter}}$ exerted on a single particle p by the surrounding fluid is related to the interphase exchange term in Eq. 2 by

$$\mathbf{F}^{\text{inter}} = \sum_{p=1}^{n_p} \xi(|\mathbf{x} - \mathbf{x}_p|) \mathbf{f}_p^{\text{inter}}, \quad (8)$$

where n_p is the total number of particles, ξ is the filtering kernel used to volume filter the Navier-Stokes equations, \mathbf{x}_p is the position of the p^{th} particle, and $\mathbf{f}_p^{\text{inter}}$ is approximated by

$$\mathbf{f}_p^{\text{inter}} \approx \mathcal{V}_p \nabla \cdot \boldsymbol{\tau} + \mathbf{f}_p^{\text{drag}}, \quad (9)$$

where \mathcal{V}_p is the volume of the p^{th} particle. The drag force is given as

$$\frac{\mathbf{f}_p^{\text{drag}}}{m_p} = \frac{1}{\tau_p}(\mathbf{u}_f - \mathbf{u}_p)F(\varepsilon_f, \text{Re}_p), \quad (10)$$

where the particle response time τ_p derived from Stokes flow is

$$\tau_p = \frac{\rho_p d_p^2}{18\mu\varepsilon_f}. \quad (11)$$

The dimensionless drag force coefficient of Tenneti et al. (2011) is employed in this work. Particle-particle and particle-wall collisions are modeled using a soft-sphere approach originally proposed by Cundall and Strack (1979). To simulate a fully-developed turbulent flow, periodic boundary conditions are used in the streamwise direction. In order to maintain a constant flow rate in this wall-bounded periodic environment, momentum is forced using a uniform source term that is adjusted dynamically in Eq. 2. To study the detailed mesoscale physics of slurries in horizontal pipes, the mathematical description presented heretofore is implemented in the framework of the NGA code (Desjardins et al., 2008). The Navier-Stokes equations are solved conservatively on a staggered grid with second order spatial accuracy for both the convective and viscous terms, and the second order accurate semi-implicit Crank-Nicolson scheme is implemented for time advancement. The details on the mass, momentum, and energy conserving finite difference scheme are given by Desjardins et al. (2008). The particles are distributed among the processors based on the underlying domain decomposition of the liquid phase. For each particle, its position, velocity, and angular velocity are solved using a second-order Runge-Kutta scheme. Coupling between the liquid phase and solid particles appears in the form of the volume fraction ε_f , and interphase exchange term $\mathbf{F}^{\text{inter}}$. These terms are first computed at the location of each particle, using information from the fluid, and are then transferred to the Eulerian mesh. To interpolate the fluid variables to the particle location, a second order trilinear interpolation scheme is used. To extrapolate the particle data back to the Eulerian mesh in a computationally efficient manner that is consistent with the mathematical formulation, a two-step mollification/diffusion operation is employed. This strategy has been shown to be both conservative and convergent under mesh refinement (Capecelatro and Desjardins, 2013a). A proper parallel implementation makes simulations

consisting of $\mathcal{O}(10^8)$ Lagrangian particles possible, allowing for a detailed numerical investigation of slurries with realistic physical parameters.

The liquid-phase transport equations are discretized on a uniform cartesian mesh, and a conservative immersed boundary (IB) method is employed to model the cylindrical pipe geometry without requiring a body-fitted mesh. The method is based on a cut-cell formulation that requires rescaling of the convective and viscous fluxes in these cells, and provides discrete conservation of mass and momentum. Details on coupling the IB method with the Lagrangian particle solver can be found in Capecelatro and Desjardins (2013a).

3. Flow configuration and simulation set-up

The configuration considered in this work is that of a liquid-solid flow through a horizontal pipe. The experimental data reported in Dahl et al. (2003) form the basis for these simulations. In the experiments, sand is injected at a rate of 2.2g/s. The properties of the sand particles are given in the table 2. The data available include the sand hold-up at different liquid flow rates as shown in figure 1 and the streamwise pressure gradient driving the flow. To set-up the numerical simulations consistent with these experiments, the number of particles are computed using the sand hold-up data as discussed below.

The sand hold-up is defined as percentage area of the pipe cross-section occupied by the static bed. It is calculated as

$$H = \frac{1}{2\pi} [2\delta - \sin(2\delta)] \quad (12)$$

where the angle, $\delta = \cos^{-1}(1 - 2h_s/D)$, and h_s is the static bed height as represented by the height of the region I in figure 1(b). Assuming the bed height is constant, the total mean volume fraction of the particles is given by

$$\langle \varepsilon_p \rangle = 0.63H + \langle \varepsilon_p^{ab} \rangle (1 - H) \quad (13)$$

where $\langle \varepsilon_p^{ab} \rangle$ denotes the mean volume fraction above the bed. Here, $\langle \rangle$ denotes time averaging. It was assumed that the particles above the bed are transported at the bulk velocity of the liquid. Below the critical deposition velocity ($U_{critical}$), relatively fewer particles get resuspended. So, this assumption is justifiable. This, however, leads to higher particle mass flow rate

when the liquid velocity is above $U_{critical}$. With this approximation, $\langle \varepsilon_p^{ab} \rangle$ can be computed as

$$\langle \varepsilon_p^{ab} \rangle \approx \frac{\dot{m}_p}{\rho_p U_{sf} A} \quad (14)$$

where \dot{m}_p is the sand injection rate. The number of particles can then be calculated from

$$\langle \varepsilon_p \rangle \frac{\pi}{4} D^2 L_x = N_p \frac{\pi}{6} d_p^3 \quad (15)$$

where L_x is the domain size in the streamwise direction, N_p is the number of particles, D is the pipe diameter, and d_p is the particle diameter.

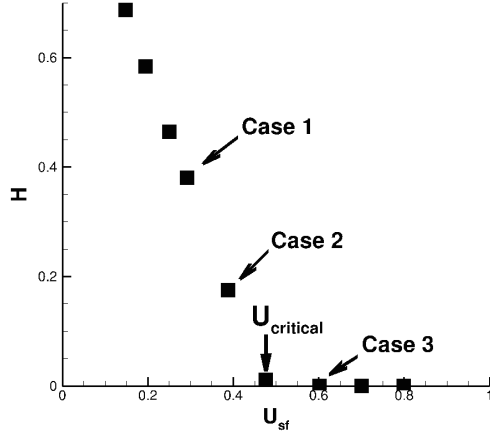
The computational domain is randomly distributed with the number of particles calculated above. To obtain initial conditions, the simulation is run by disregarding the hydrodynamic forces. This allows only the gravity and particle-particle collision forces to act on the the particles that will eventually result in a static bed. Then the fluid-particle interaction is activated by specifying superficial liquid velocity consistent with the experiments. As the liquid flow rate increases, the particles get eroded from the static bed and get transported along with the carrier liquid. Using the mean particle velocity, the particle mass flow rate can be computed and compared with the sand injection rate as a consistency check.

Due to the high Reynolds numbers considered in this work, our investigation is currently restricted to only three cases to assess the capability of Euler-Lagrange LES approach to predict the slurry flow physics. The particular cases considered are presented in the table 1 and flow parameters are given in table 2.

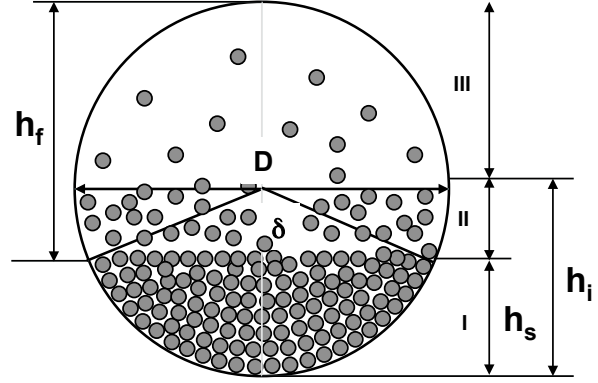
Case	$U_{sf}(\text{m/s})$	Re_{sf}	N_p
1	0.3	20700	19.25×10^6
2	0.4	27600	8×10^6
3	0.6	41400	0.042×10^6

Table 1: Different cases considered, see also in figure 1(a). N_p is the number of particles and Re_{sf} is Reynolds number based on superficial velocity and pipe diameter.

The computational grid used has $768 \times 156 \times 156$ points in the streamwise (X), wall-normal (Y), and spanwise (Z) directions respectively. To capture the mesoscale features in this flow, each cell size is chosen to be equal to twice the particle diameter. The length of the domain is chosen to be long enough



(a) Sand hold-up data



(b) A schematic showing static bed of particles

Figure 1: Sand hold-up data from the experiments by Dahl et al. (2003). The three cases considered for the simulations are shown by arrows. $U_{critical}$ is the critical deposition velocity and h_f is the fluid height. Three distinct regions as observed in Capecelatro and Desjardins (2013b): I denotes static bed region, II denotes intermediate region with erosion and deposition as dominant processes, and III denotes region with fully entrained particles. Note that height of the static bed region is denoted as h_s and the height of the liquid-bed interface is denoted as h_i . For exact definitions of these heights, see section 4.1.

Pipe diameter, D	0.069 m
Particle diameter, d_p	280×10^{-6} m
Particle density, ρ_p	2650 kg/m ³
Liquid density, ρ_f	998 kg/m ³

Table 2: Flow parameters

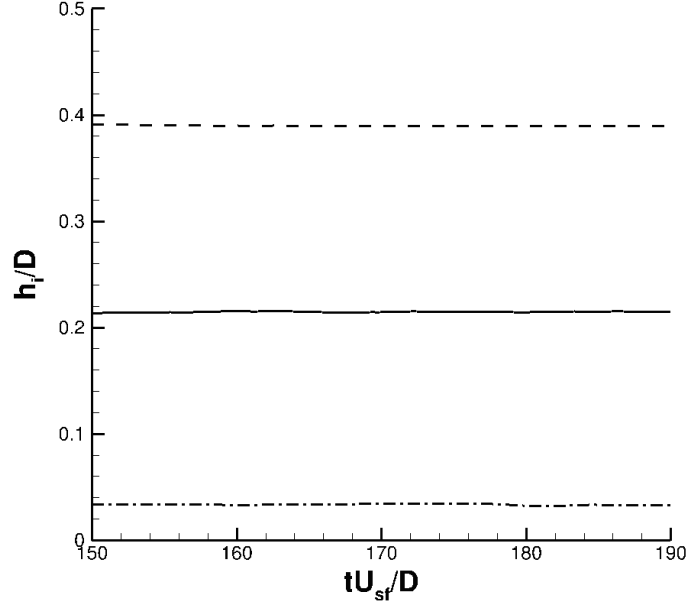


Figure 2: Convergence history showing mean height of the liquid-bed interface

for the simulations to be computationally tractable. Streamwise periodic boundary condition is enforced to get fully developed flow. The simulations are run for approximately 150 inertial time scales given by tU_{sf}/D where U_{sf} is the superficial liquid velocity and D is the pipe diameter. The statistics are extracted over another 40 time scales. The convergence of the simulations in terms of the mean height of the liquid-bed interface is shown in the figure 2.

4. Results and discussion

Due to the high cost of the simulations, the discussion of results will be limited to the first-order statistics such as mean velocity and mean concentration.

4.1. Global statistics

The pressure gradient driving the flow from numerical simulations is compared with the experimental data from Dahl et al. (2003) as given in table 3. The agreement with the experiments is within 10%. This slight discrepancy could be attributed to the assumptions used in the configuration set-up. As given in the table, the average particle mass flow rate calculated from the

simulations is of the same order of magnitude, although systematically larger than the sand injection rate given in the experiments (2.2g/s). The pressure gradient driving the flow decreases with decrease in the superficial liquid velocity. When the liquid flow rate decreases, the sand particles tend to get deposited more at the bottom, which in turn increases the pressure gradient again. This non-monotonic behavior seems to have been reproduced by the present approach.

Case	U_{sf}	$(dp/dx)_{exp}$	$(dp/dx)_{LES}$	\dot{m}_p
1	0.3	80.807	71.5	3.8
2	0.4	61.741	70.4	3.2
3	0.6	72.59	74.64	4.2

Table 3: Pressure gradient at different superficial liquid velocities in the units of (Pa/m). \dot{m}_p is the average particle mass flow rate in the units of (g/s) and U_{sf} is the superficial liquid velocity in the units of (m/s).

To further verify our computational approach, the sand hold-up is computed *a posteriori* from the simulations using equation 1(b). The results are presented in the table 4. The predicted values are in good agreement with the data. Since we set-up simulations based on the hold-up data from experiments, as the particles get resuspended, the hold-up decreases from the experimental value, as expected. We predict zero hold-up for case 3 in agreement with the data. To predict $U_{critical}$ from the simulations, the data points below $U_{critical}$ are extrapolated linearly to the axis representing zero hold-up (see figure 3). This gives $U_{critical}$ from the simulations to be 0.46m/s, which is within 3% of the experimental value.

Case	$U_{sf}(\text{m/s})$	H_{exp}	H_{LES}	h_s	h_i
1	0.3	0.362	0.341	$92d_p$	$96d_p$
2	0.4	0.150	0.127	$45d_p$	$53d_p$
3	0.6	0.000	0.000	0.0	$8d_p$

Table 4: Sand hold-up comparison with experimental data.

The location of the interface between the liquid and the particle bed is defined in two ways. Following Kidanemariam and Uhlmann (2014), the

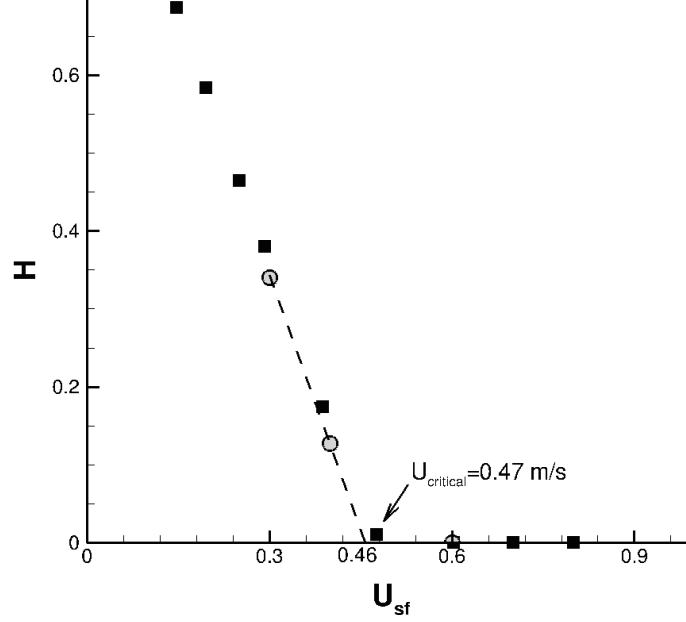


Figure 3: Comparison of the sand hold-up predictions with the data. Squires: Experiments of Dahl et al. (2003), circles: Euler-Lagrange LES.

height of the interface is calculated using a threshold value $\langle \varepsilon_p \rangle_z = 0.1$ as

$$h_i(x, t) = y|_{\langle \varepsilon_p \rangle_z = 0.1} \quad (16)$$

where $\langle \rangle_z$ represents spanwise averaging over a few cells near the centerline of the pipe. The mean liquid-bed interface height (h_i) can be calculated by further averaging in the streamwise direction and in time. This corresponds to the height of the regions I and II combined as shown in the figure 1(b). This definition is relevant for plotting the liquid phase velocity, as presence of particles above the bed increase the viscosity and hence attenuate turbulence. So, the viscous sublayer for the liquid phase extends farther away from the static bed. The other definition used is the height of the static bed. It is defined as

$$h_s(x, t) = y|_{\langle u_p \rangle_z = 0.01 U_{sf}} \quad (17)$$

A mean value for the static bed height (h_s) can be obtained by performing averaging in the streamwise direction and in time. This corresponds to the height of region I shown in figure 1(b). The static bed height is relevant for plotting the vertical profiles of the particle phase. These two heights are

presented in the table 4. The difference in the heights represent a region of the particles where erosion and deposition are the dominant processes. In case 1, this region is $4d_p$, whereas for the other two cases, it is $8d_p$.

4.2. Mean flow profiles

The vertical profiles of the first-order statistics presented in this section are extracted at the pipe centerline ($Z = 0$), averaged in the streamwise direction and in time.

In annular liquid-gas flows, McCaslin and Desjardins (2014) showed that gas velocity profiles normalized in interface units recover single-phase law of the wall behavior. This is interesting observation for the modeling considerations. Motivated by this, the mean liquid velocity normalized in the units of liquid-bed interface are plotted in the figure 4 from our current simulations. Note that the profiles are plotted in shifted coordinates using the liquid-bed interface height (h_i) and the velocity is normalized using friction velocity calculated at this interface. There is viscous sublayer for all the cases, but the log-law behavior is found to be very different. This could be due to the complex particle dynamics and four-way coupling.

The mean particle velocity and concentration profiles (shown in figures 5 and 6) are plotted in normalized units of static bed height (h_s). The profiles show that the particles are transported in a thin layer in case 1, whereas transport happens in a much thicker layer for the other two cases. For cases 2 and 3, both velocity and concentration profiles show similar behavior. Case 1 shows much steeper concentration gradients above the bed.

4.3. Characterizing the transport layer thickness

The thickness of the layer in which the particles are being transported is an important parameter from the engineering analysis point of view. Following Durán et al. (2012), the characteristic transport layer thickness λ can be defined as

$$\lambda = \left(\frac{\int_0^\infty (y - \bar{y})^2 \langle u_p \rangle(y) dy}{q} \right)^{1/2} \quad (18)$$

where $\bar{y} = \frac{1}{q} \int_0^\infty y \langle u_p \rangle(y) dy$ gives the altitude of the transport layer centre, $q = \int_0^\infty \langle u_p \rangle(y) dy$ is the volume flux of the particles, and $\langle \rangle$ denote averaging in the streamwise direction and in time. The transport layer thickness calculated is presented in the table 5. As expected, transport in the lowest liquid flow rate case happens in a thin layer of the order of few particle diameters.

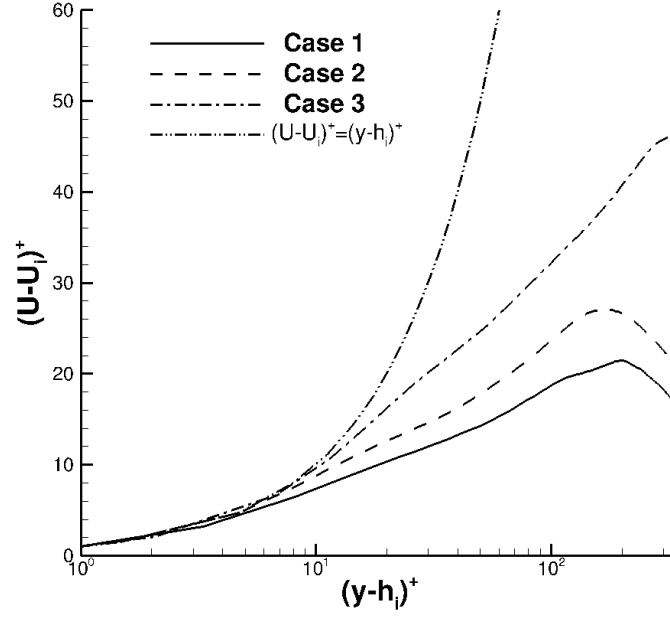


Figure 4: Mean liquid velocity profiles plotted in the interface units

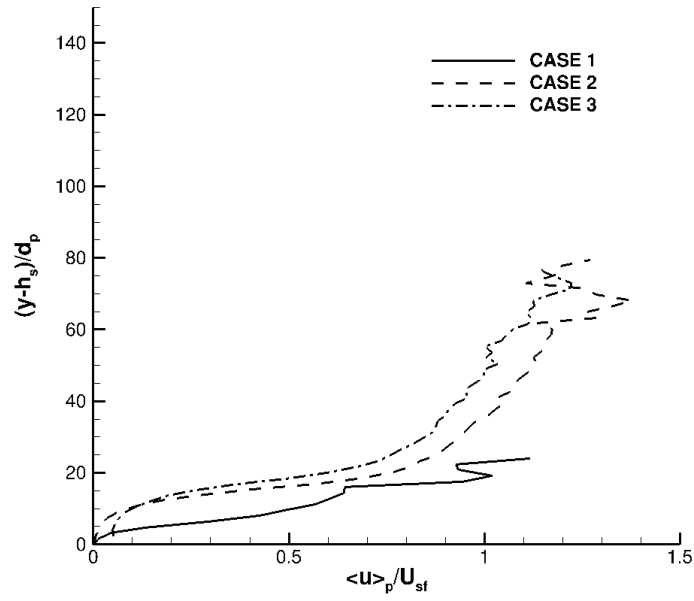


Figure 5: Mean particle velocity profiles

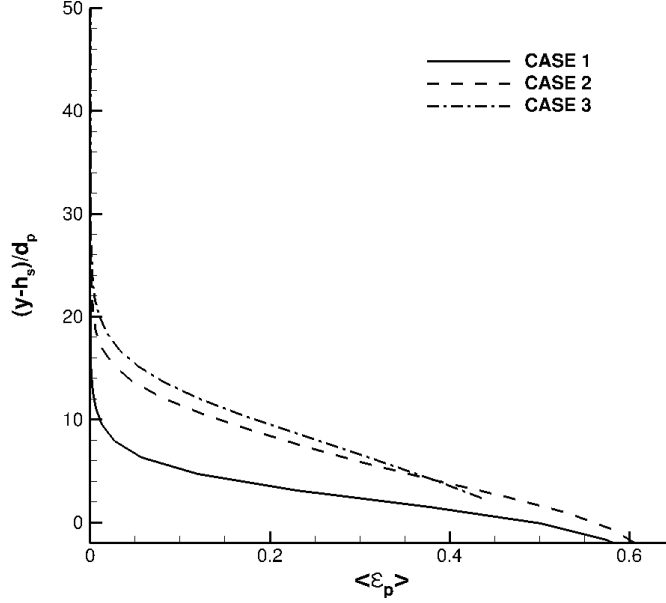


Figure 6: Mean particle concentration profiles

When the liquid flow rate is increased, the layer thickness increases. This is consistent with the mean particle velocity profiles presented in the section 4.2.

Case	$U_{sf}(\text{m/s})$	λ
1	0.3	$9d_p$
2	0.4	$14d_p$
3	0.6	$11d_p$

Table 5: Transport layer thickness

4.4. Pattern formation and relevance of phase diagrams

Another interesting question to address is the relevance of phase diagrams presented in the literature to explain the pattern formation above the static bed. The formation of ripples/dunes is widely reported in the sediment transport literature in the form of Shields diagram. To represent the current simulations within this diagram, the Shields parameter, θ , needs to

be calculated. The classical definition of θ is

$$\theta = \frac{\tau_b}{(\rho_p - \rho_f)gd_p} \quad (19)$$

where τ_b is the bed shear stress.

From Euler-Lagrange simulations, the bed shear stress (τ_b) can be inferred through multiple strategies. Using friction velocity calculated from the Eulerian velocity field, the bed shear stress is calculated as

$$\tau_b = \mu^* \left. \frac{\partial U}{\partial y} \right|_{h_i} \quad (20)$$

where U is the mean liquid velocity as shown in figure 4.

The Shields parameter aims at providing an estimate of the relative magnitude of the streamwise and vertical forces, which is readily available in the present Lagrangian treatment of the particles. So, the following definition can be used to extract the bed shear stress from Lagrangian data:

$$\tau_b = \langle f_{p,x}^{inter} \rangle_t / A_{projected} \quad (21)$$

where $A_{projected}$ for a spherical particle is $(\pi/4)d_p^2$ and $\langle \rangle_t$ denotes time averaging.

The Shields number computed using Eulerian data using equation 20 is denoted as θ_e and the Lagrangian data using equation 21 is denoted as θ_l . The calculated values for this parameter are presented in the table 6. It shows that θ calculated using both the definitions are consistent. The Shields number computed using the Lagrangian data directly represents the forces felt by the particles near the surface of the bed. We use this definition to place our simulations within the Shields diagram that is shown in figure 7. Shields curve represented as a solid line denotes the threshold for incipient sediment motion. Curves showing Bagnold (1966) and Van Rijn (1984) denote initiation of the suspended load. Particular bedform is determined by the dotted line plotted at $\theta = 0.8$, below which the data indicates formation of ripples/dunes. Note that all three simulations fall in this regime, hence dune formation is expected from the Shields diagram.

Shields parameter is primarily meant for predicting the incipient motion of the sediment particles. So, Ouriemi et al. (2009b) plotted a phase diagram in the $Re-Ga(h_f/d_p)^2$ plane to explain the pattern formation specific to the pipe flow. In this plane, the Galileo number, $Ga = d^3(\rho_p - \rho_f)g/\nu$, used is the

Case	U_{sf} (m/s)	θ_e	θ_l
1	0.3	0.0961	0.110
2	0.4	0.0722	0.071
3	0.6	0.1071	0.119

Table 6: Shields parameter calculated from Eulerian and Lagrangian data.

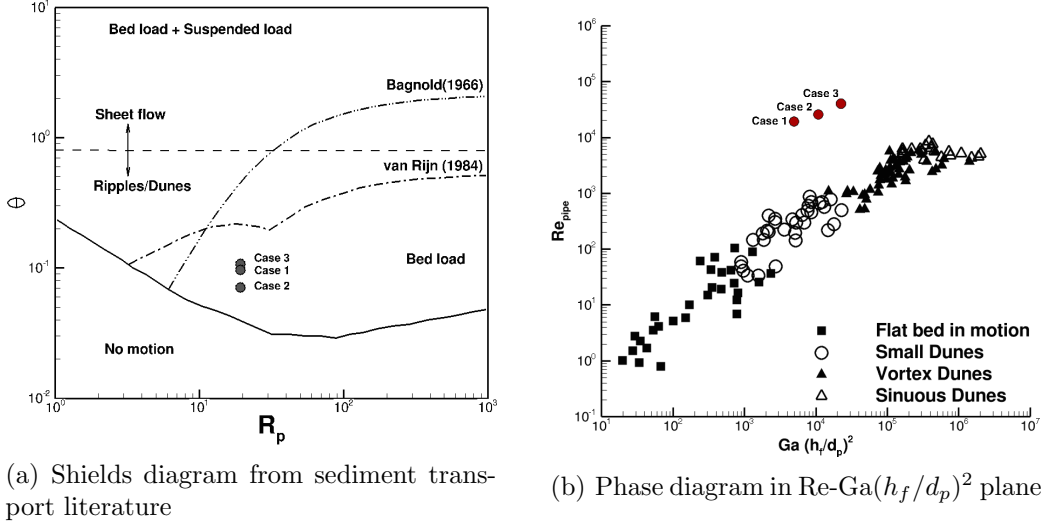


Figure 7: Phase diagrams from experimental observations.

Reynolds number based on the Stokes settling velocity of the particles. This is analogous to the fall parameter on the Shields diagram. The experiments are performed up to Reynolds number of 5800, whereas the present simulations are conducted at significantly higher Reynolds numbers. With reference to the abscissa, the lowest liquid flow rate corresponds to small dunes regime. At higher flow rates, “vortex dunes” are expected based on this diagram.

With the understanding gained from phase diagrams, a plausible explanation for the pattern formation emerges. The incipient erosion of the particle bed is determined by the bed shear stress. Once the particles are eroded, the particle-particle collisions play a dominant role in feeding the particles to the vortical structures in the turbulent flow leading to different patterns above the static bed.

Instantaneous snapshots of the particle configuration are plotted in the

figures 8-10. At low liquid flow rates, only a small amplitude dunes are formed as evident from the side view in figure 8. As the flow rate is increased, the ridges and troughs are more clearly visible in the side view for both case 2 and 3 as shown in figures 9-10. For case 3 with the highest liquid flow rate, the patterns show that there are regions at the bottom of the pipe where there are no particles (in the troughs). This is consistent with the experimental observations of Ouriemi et al. (2009b).

To further understand and characterize the type of dunes, we have plotted vortical structures identified through iso-surfaces of Q -criterion in figure 11. The Q -criterion is used to identify a vortex as a region where the rate of rotation is greater than the rate of strain (Hunt et al., 1988) and is defined as

$$Q = (|\mathbf{\Omega}|^2 - |\mathbf{S}|^2) > 0 \quad (22)$$

where $\mathbf{\Omega}$ is the rate of rotation tensor and \mathbf{S} is the rate of strain tensor. In the case 1, there are only small amplitude dunes and hence the vortical structures do not seem to have been influenced by these patterns. In the case 2, however, vortical structures are coupled to the dune formation. These coherent structures essentially indicate flow separation in the troughs. As reported in Ouriemi et al. (2009b), the dune patterns observed in case 2 can be denoted as “vortex dunes”. Case 3 also shows vortical structures, but the particles are present very close to the bottom wall of the pipe, it is difficult to visualize the structures above the dune patterns.

The formation of small dunes for case 1, and formation of vortex dunes for the other two cases show that the present simulations reproduce the expected behavior from the phase diagrams.

4.5. Space-time evolution of the liquid-bed interface

To understand the space-time evolution of the patterns, the fluctuation in the height of liquid-bed interface is calculated using

$$h'(x, t) = h_i(x, t) - \langle h_i \rangle_x(t) \quad (23)$$

where $\langle \rangle_x$ denotes averaging in the streamwise direction. Space-time plots of h' are shown in figure 12. The ridges and troughs that are observed in this figure indicate dune formation. In the lower liquid flow rate case, the fluctuations in the height of the liquid-bed interface are weak. For the other two cases, the fluctuations are strong. The propagation speed of the patterns can be calculated by looking at the slope of the line determined by



Figure 8: Top and side views of the instantaneous particle configuration for case 1, colored by the particle velocity.

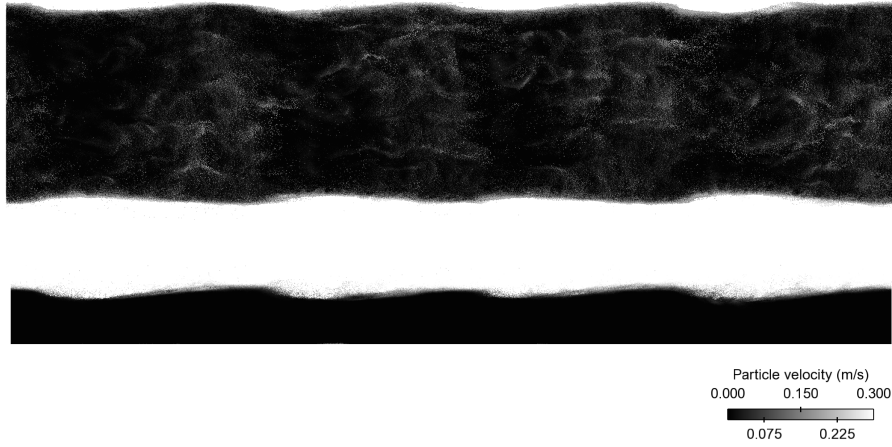


Figure 9: Top and side views of the instantaneous particle configuration for case 2, colored by the particle velocity.

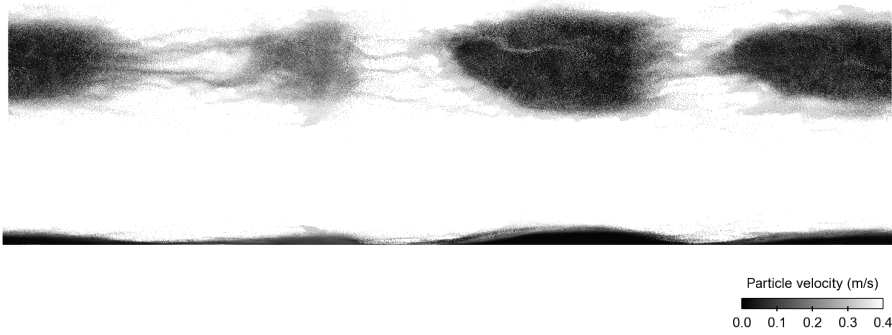


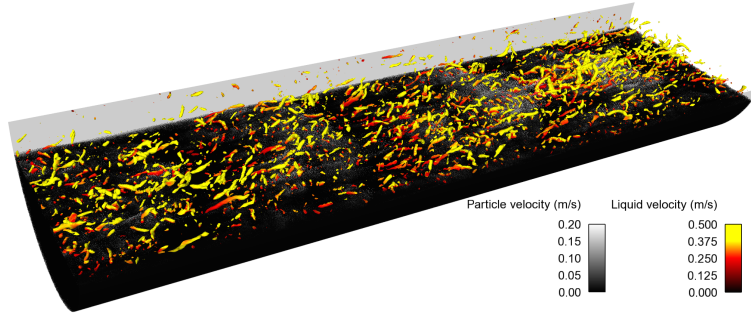
Figure 10: Top and side views of the instantaneous particle configuration for case 3, colored by the particle velocity.

the locus of the maximum of the height of the liquid-bed interface. In the final period of the simulation, the propagation speed in case 1 with small dunes is approximately $0.0478u_b$ whereas the case with “vortex dunes” is approximately $0.03467u_b$, where u_b is the bulk velocity of the liquid above the static bed. In case 3, the patterns exhibit interesting dynamics such as merging and branching. Measuring the dune speed in the final period for this case gave $0.054u_b$, so propagation speed is highest in the case with the largest liquid flow rate.

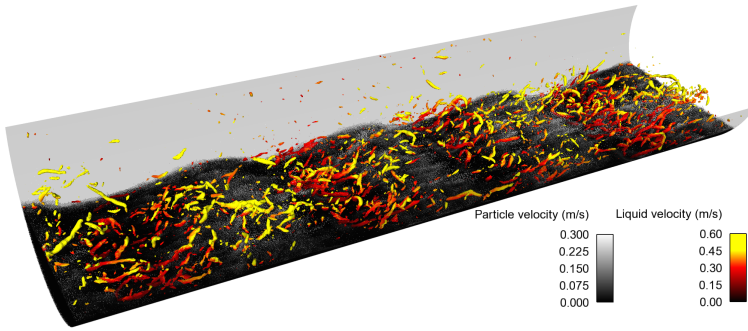
5. Concluding remarks

The dynamics of liquid-solid slurry flows through a horizontal pipe have been investigated using a highly resolved Euler-Lagrange LES strategy. It was found that depending on the liquid flow rate, particles exhibit different patterns that are consistent with the existing literature. The evolution of these patterns in space and time is presented and the propagation speed is calculated. The mean streamwise pressure gradient from numerical simulations agree with the experiments within engineering accuracy levels. The vertical profiles for the mean particle velocity and concentration are extracted from the simulations and presented.

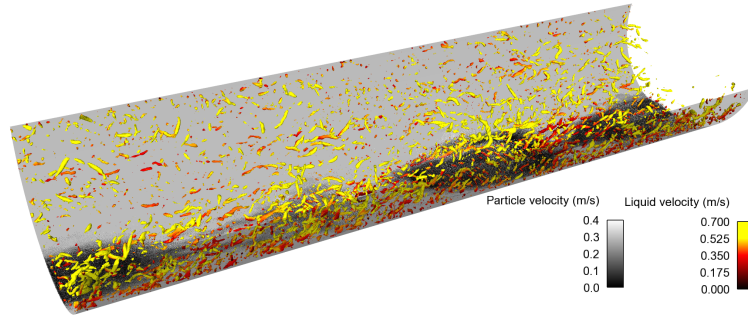
These simulations show that Euler-Lagrange LES can be used as a viable tool in gaining physical insight of such complex liquid-solid flows. To our knowledge, this is the first work demonstrating the capability of accurately



(a) Case 1



(b) Case 2



(c) Case 3

Figure 11: Vortical structures detected using iso-surfaces of Q-criterion

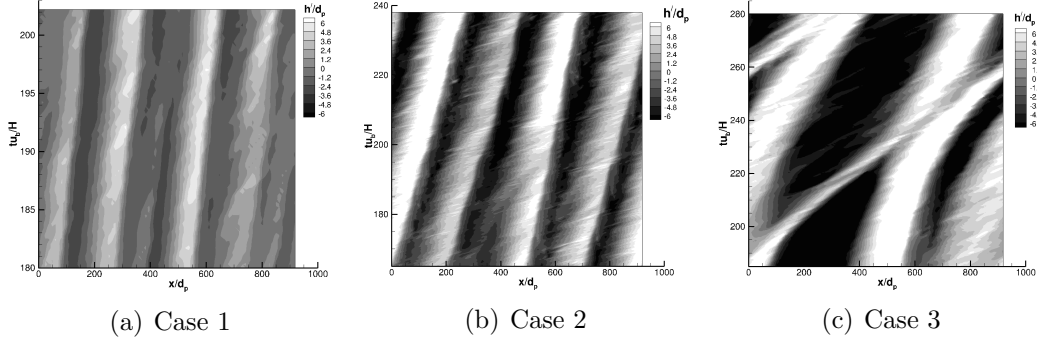


Figure 12: Space-time diagram showing evolution of the patterns.

predicting the critical deposition velocity. Further investigation include extracting detailed statistics from these simulations to aid in the process of developing improving fluid-particle closure models used in the Euler-Euler formalism.

References

- Bagnold, R. A., 1966. An approach to the sediment transport problem from general physics. Geological Survey Professional Paper 422-I.
- Buffington, J. M., Montgomery, D. R., 1997. A systematic analysis of eight decades of incipient motion studies, with special reference to gravel-bedded rivers. *Water Resources Research* 33 (8), 1993–2029.
- Capecelatro, J., Desjardins, O., 2013a. An Euler–Lagrange strategy for simulating particle-laden flows. *Journal of Computational Physics* 238, 1 – 31.
- Capecelatro, J., Desjardins, O., 2013b. Eulerian–Lagrangian modeling of turbulent liquid–solid slurries in horizontal pipes. *International Journal of Multiphase Flow* 55, 64 – 79.
- Charru, F., 2006. Selection of the ripple length on a granular bed sheared by a liquid flow. *Physics of Fluids* 18 (121508), 1–9.
- Church, M., 2006. Bed material transport and the morphology of alluvial river channels. *Annual Review of Earth and Planetary Sciences* 34 (1), 325–354.

- Coleman, S., Nikora, V. I., 2009. Bed and flow dynamics leading to sediment-wave initiation. *Water Resources Research* 45 (4), 1–12.
- Cundall, P., Strack, O., 1979. A discrete numerical model for granular assemblies. *Geotechnique* 29 (1), 47–65.
- Dahl, A. M., Ladam, Y., Unander, T., Onsrud, G., 2003. SINTEF-IFE Sand transport 2001-2003. In: SINTEF Internal Report.
- Dancey, C. L., Diplas, P., Papanicolaou, A., Bala, M., 2002. Probability of individual grain movement and threshold condition. *Journal of Hydraulic Engineering* 128 (12), 1069–1075.
- Danielson, T. J., 30 April - 3 May 2007. Sand transport modeling in multiphase pipelines. Houston, Texas, U.S.A.
- Desjardins, O., Blanquart, G., Balarac, G., Pitsch, H., 2008. High order conservative finite difference scheme for variable density low Mach number turbulent flows. *Journal of Computational Physics* 227 (15), 7125–7159.
- Durán, O., Andreotti, B., Claudin, P., 2012. Numerical simulation of turbulent sediment transport, from bed load to saltation. *Physics of Fluids (1994-present)* 24 (10), 103306.
- Germano, M., Piomelli, U., Moin, P., Cabot, W. H., 1991. A dynamic subgrid-scale eddy viscosity model. *Physics of Fluids A: Fluid Dynamics* 3, 1760.
- Gibilaro, L., Gallucci, K., Di Felice, R., Pagliai, P., 2007. On the apparent viscosity of a fluidized bed. *Chemical engineering science* 62 (1-2), 294–300.
- Hunt, J. C. R., Wray, A., Moin, P., 1988. Eddies, stream, and convergence zones in turbulent flows. Center for Turbulence Research Report CTR-S88.
- Jenkins, J. T., Hanes, D. M., 9 1998. Collisional sheet flows of sediment driven by a turbulent fluid. *Journal of Fluid Mechanics* 370, 29–52.
- Kidanemariam, A. G., Uhlmann, M., 2014. Direct numerical simulation of pattern formation in subaqueous sediment. *Journal of Fluid Mechanics* 750 (R2), 1–13.

- Langlois, V., Valance, A., 2007. Initiation and evolution of current ripples on a flat sand bed under turbulent water flow. *The European Physical Journal E: Soft Matter and Biological Physics* 22 (3), 201–208.
- Lilly, D., 1992. A proposed modification of the Germano subgrid-scale closure method. *Physics of Fluids A: Fluid Dynamics* 4, 633.
- McCaslin, J. O., Desjardins, O., 2014. Numerical investigation of gravitational effects in horizontal annular liquid-gas flow. *International Journal of Multiphase Flow* 67, 88–105.
- Meneveau, C., Lund, T., Cabot, W., 1996. A Lagrangian dynamic subgrid-scale model of turbulence. *Journal of Fluid Mechanics* 319 (1), 353–385.
- Nielsen, P., 1992. Coastal bottom boundary layers and sediment transport. *Advanced Series on Ocean Engineering: Volume 4*. World Scientific.
- Ouriemi, M., Aussillous, P., Guazzelli, E., 2009a. Sediment dynamics. Part 1. Bed-load transport by laminar shearing flows. *Journal of Fluid Mechanics* 636, 295–319.
- Ouriemi, M., Aussillous, P., Guazzelli, E., 2009b. Sediment dynamics. Part 2. Dune formation in pipe flow. *Journal of Fluid Mechanics* 636, 321–336.
- Ouriemi, M., Aussillous, P., Medale, M., Peysson, Y., Guazzelli, É., 2007. Determination of the critical Shields number for particle erosion in laminar flow. *Physics of Fluids* 19 (6), 61706–63100.
- Paintal, A., 1971. Concept of critical shear stress in loose boundary open channels. *Journal of Hydraulic Research* 9 (1), 91–113.
- Papnicolaou, A. N., Diplas, P., Evaggelopoulos, N., Fotopoulos, S., 2002. Stochastic incipient motion criterion for spheres under various bed packing conditions. *Journal of Hydraulic Engineering* 128 (4), 369–380.
- Peysson, Y., Ouriemi, M., Medale, M., Aussillous, P., Guazzelli, É., 2009. Threshold for sediment erosion in pipe flow. *International Journal of Multiphase Flow* 35 (6), 597–600.
- Raudkivi, A., 1997. Ripples on stream bed. *Journal of Hydraulic Engineering* 123 (1), 58–64.

- Tenneti, S., Garg, R., Subramaniam, S., 2011. Drag law for monodisperse gas-solid systems using particle-resolved direct numerical simulation of flow past fixed assemblies of spheres. *International Journal of Multiphase Flow* 37 (9), 1072–1092.
- Van Rijn, L. C., 1984. Sediment transport, Part II: Suspended load transport. *Journal of Hydraulic Engineering* 110 (11), 1613–1641.
- Vanoni, V. A., 1946. Transportation of suspended sediment by water. *Transactions of the American Society of Civil Engineers* 111, 67–113.
- Wilson, K., 1989. Friction of wave-induced sheet flow. *Coastal Engineering* 12, 371–379.
- Yalin, M. S., 1977. *Mechanics of sediment transport*. Pergamon Press.
- Yang, Z. L., Ladam, Y., Laux, H., Danielson, T. J., Leporcher, E., 2006. Dynamic simulation of sand transport in a pipeline. In: 5th North American Conference on Multiphase Technology. Banff, Canada.